Laser-Driven Plasma Loader for Shockless Compression and Acceleration of Samples in the Solid State

J. Edwards, K. T. Lorenz, B. A. Remington, S. Pollaine, J. Colvin, D. Braun, B. F. Lasinski, D. Reisman, J. M. McNaney,
J. A. Greenough, R. Wallace, H. Louis, and D. Kalantar

Lawrence Livermore National Laboratory, P.O. Box 808, Livermore, California 94550, USA

A new method for shockless compression and acceleration of solid materials is presented. A plasma reservoir pressurized by a laser-driven shock unloads across a vacuum gap and piles up against an Al sample thus providing the drive. The rear surface velocity of the Al was measured with a line VISAR, and used to infer load histories. These peaked between ~ 0.14 and 0.5 Mbar with strain rates $\sim 10^6 - 10^8$ s^{-1}. Detailed simulations suggest that apart from surface layers the samples can remain close to the room temperature isentrope. The experiments, analysis, and future prospects are discussed.

In this Letter we report on a new laser-driven technique to produce dynamic, shockless compression of materials for studying the properties of matter at high pressure and density, but low temperature. Shockless techniques allow continuous information along the compression isentrope to be obtained [1] rather than at a single point on a Hugoniot such as in a shock wave experiment [2]. Previous shockless compression techniques include graded density "pillow impactors" fired in a gas or powder gun [1,3], high explosive (HE) products expanding across a vacuum gap [4], and a temporally shaped magnetic pressure pulse [5] at the high power Z facility. The new laser based scheme discussed in this Letter is similar to the HE method, but uses a laser-driven shock wave to pressurize the reservoir, with the potential of reaching very high pressures, ~ 1 Mbar, on existing facilities. The next generations of high power drivers [the National Ignition Facility (NIF) [6] and a refurbished Z facility] are expected to be capable of quasi-isentropic compression up to ~ 10 Mbar, accessing new regimes in high-density, low-temperature material properties research, in which there is considerable theoretical interest [7]. This prospect is especially interesting for planetary science [8]. Specific examples include the phase and equation of state (EOS) of materials under conditions of the Earth's core (~ 1–4 Mbar) [9]; testing for the existence of a first order plasma phase transition in liquid hydrogen, which fundamentally influences the structure and evolution of gas giant planets such as Jupiter [10] and brown dwarfs [11]; and looking for the long predicted insulator-metal transition in solid-state hydrogen [12]. Another application is the measurement of solid-state dynamics at ultrahigh strain rates ($> 10^6$ s^{-1}) relevant to meteor impact and crater formation studies [13]. At such high strain rates the dominant resistance to deformation is hypothesized to be phonon scattering [14], a theory which is largely untested due to a

lack of experimental data. The technique we describe can also be used to create ultrahigh velocity microflyer plates, which are of potential interest for EOS studies [15] and interstellar dust dynamics [16].

The process reported here consists of three distinct phases (Fig. 1). First, a laser-driven shock wave is used to pressurize the reservoir and set it in motion with the post shock velocity. In our case, the shock is strong enough to turn the reservoir into a weakly ionized plasma. The exact state depends on the EOS of the reservoir and the shock pressure, P_s. After the shock exits the rear of the reservoir, the plasma unloads towards the sample, situated some distance away across a vacuum gap. Because the plasma is relatively cool, this phase is reasonably approximated by a classical adiabatic rarefaction wave, which stretches out the plasma in proportion to the gap size. In the final phase the reservoir plasma piles up against the sample thereby producing a smoothly increasing applied pressure (the load) as it converts its kinetic energy into thermal pressure. It can be shown that the maximum load is up to $\sim 3P_s$ [17]. The compression
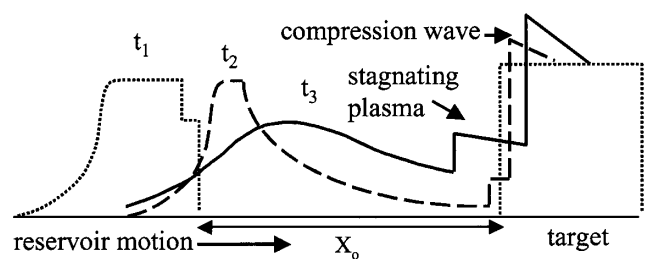

FIG. 1. Schematic of target density at three times: t_1 the shock is about to break out of the reservoir; t_2, the reservoir has unloaded across the gap and is starting to pile up against the sample initiating the shockless compression wave; t_3, the reservoir continues to rarefy, the load is increasing, and the wave in the sample is beginning to steepen.
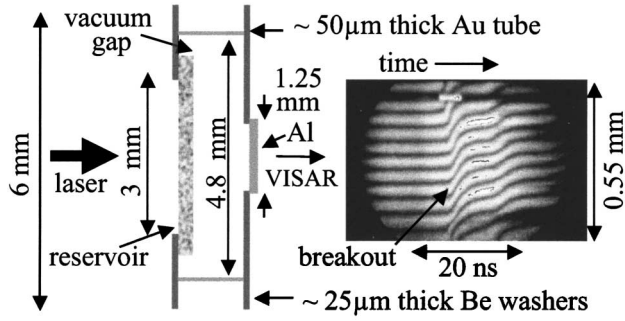
FIG. 2. Schematic of the target, and a typical VISAR record reflected from the rear of a 29.4 μm Al foil (Table I, B). Fringe motion indicates acceleration of the surface (1.65 km/s/ fringe). Targets were axisymmetric about the laser axis.

wave that is launched into the sample gradually steepens with distance traveled and eventually breaks into a shock wave. The depth at which this happens sets the maximum useful sample thickness.

A schematic of the target together with typical dimensions is shown in Fig. 2 (side view). Details for the four specific shots we present here are given in Table I. The reservoir and sample were supported on Be washers, mounted on either end of a precision-machined gold tube. The diameters of these components were very oversized to completely rule out edge effects and reservoir plasma getting around the target and impacting the rear of the sample. Reservoirs were either $\sim$0.3 mm thick carbonized resorcinol formaldehyde foam [18] of density 0.1 g/cm^3, or $\sim$0.2 mm thick solid plastic $\sim$1.2 g/cm^3. Samples were Al and ranged in thickness from $\sim$10–30 μm. On one shot (D, Table I) the Al was backed by $\sim$135 μm of LiF which is very well impedance matched to the Al so that the entire sample acts like a thick block of Al. The LiF remains transparent to the VISAR throughout the experiment, which means we always reflect off the rear surface of the Al, effectively measuring the particle velocity in the wave as opposed to the free surface velocity.

The reservoir shock was generated by a number of Omega laser [19] beams (0.35 μm wavelength) focused onto the front surface of the reservoir at intensities of $\sim$(1–10) $\times$ 10^{12} W cm^{-2} for 3.7–7.4 ns. Phase plates were used to smooth the beams resulting in an on target focal spot profile such that the intensity remained within 90% of its peak value over a diameter of $\sim$0.6 mm ($\sim$0.8 mm FWHM) at best focus [20], or $\sim$1.4 mm ($\sim$2.3 mm FWHM) in defocused mode. The principal diagnostic was a line VISAR [21] used to image the rear surface of the Al and measure its velocity with a sensitivity of 1.65 km/s/fringe. Temporal resolution ($\sim$0.15 ns) was provided by an optical streak camera and the spatial resolution was $\sim$20 μm. The VISAR record for case B (Table I) is shown in Fig. 2. The initial rise in the velocity (upward deflection of fringes after breakout in Fig. 2) is determined by the shape of the incoming compression wave, which is set by the temporal shape of the load, and the EOS and thickness of the sample. The subsequent fringe motion results from a combination of the acceleration of the sample as a whole, superposed with smooth steps due to waves reverberating back and forth within the sample. Through all of this the fringe motion is smooth and continuous indicating that the sample remained in tact, and that no shocks, which would result in sharp discontinuities in the fringes, were present.

The measured velocity from each shot [Fig. 3(a)] can be used to derive the load history at the front surface of each sample. The procedure to do this consists of back-integrating in space the equations of hydrodynamics neglecting dissipation, with an assumed EOS, using the rear surface velocity history as the initial condition [22]. This is done directly from the measured velocity data and is valid provided that the EOS of the sample is known, which is the case for Al under these conditions, and that the flow is isentropic. Material strength introduces dissipative terms, but these appear to be negligible for the cases studied here (see below).

To check that the $P_L(t)$ calculated in this way were reasonable we input them into the hydrocode LASNEX

TABLE I. E = laser energy, I_{12} = laser intensity (10^{12} W cm^{-2}) defined by $E = 2\pi I_{12} \int r\tilde{I}(r)dr$ where $\tilde{I}(r)$ is the normalized on target intensity profile, t_p = laser pulse length, ϕ = focal spot FWHM, X_R = reservoir thickness, X_G = gap width, X_{Al} = Al thickness, P_L = peak load, P_c, $\dot{\varepsilon}_c$, η_c, T_c = peak pressure, strain rate, compression, and temperature in the center of the sample. T_c/T_m = fraction of melt temperature.

	E (kJ)	I_{12}	t_p (ns)	ϕ (mm)	X_R (mm)	X_G (mm)	X_{Al} (μm)	P_L (Mbar)	$\dot{\varepsilon}_c$ (10^7 s^{-1})	P_c (Mbar)	η_c	T_c (K)	T_c/T_m
A[a]	0.19	3.2	7.4	0.8	0.27	0.38	16.5	0.51	6	0.47	1.36	470	0.16
B[a]	0.87	5.1	3.7	2.3	0.3	0.43	29.4	0.33	2	0.26	1.24	406	0.20
C[b,c]	1.4	8.2	3.7	2.3	0.2	0.3	24.0	0.14	0.5	0.14	1.14	360	0.19
D[d]	0.22	7.5	3.7	0.8	0.17	0.29	22.0	0.16	0.5	0.09	1.09	331	0.21

[a]0.1 g/cm^3 foam reservoir.
[b]Composite reservoir: 20 μm polycarbonate (C$_{16}$H$_{16}$O$_4$, 1.2 g/cm^3) + 180 μm brominated polystyrene (C$_{50}$H$_{48}$Br$_2$, 1.23 g/cm^3).
[c]Al was backed by 135 μm LiF.
[d]Polycarbonate reservoir.

[23] and compared the simulated Al rear surface velocities with those measured experimentally. In all cases the LASNEX results were indistinguishable from the experiment, validating the procedure. We also found no noticeable difference in the simulated rear surface velocities whether a strength model was included in the calculations or not. The backintegrated loads are shown in Fig. 3(b). Time, $t = 0$, is taken to be the instant loading at the front surface of the sample commences. Since the
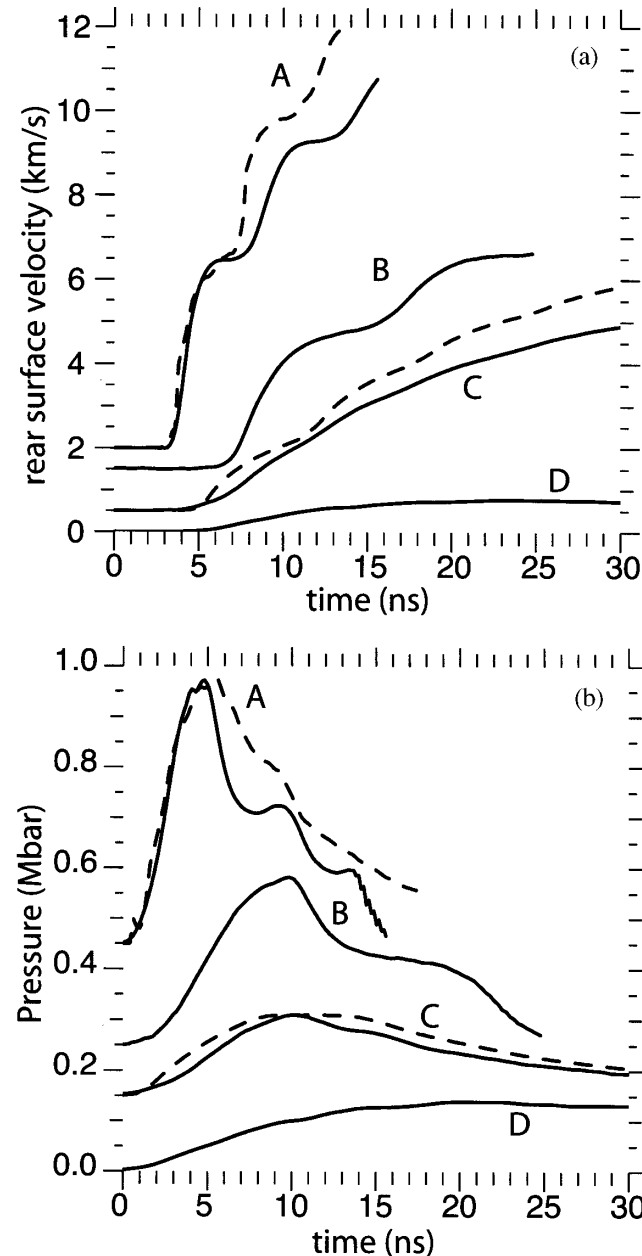

FIG. 3. (a) Rear surface velocity data for the experiments listed in Table I, and the associated backintegrated front surface loads (b). Integrated LASNEX simulations (dashed lines) are shown for cases A and C. Curves A, B, and C are offset vertically by $+(2, 1.5, 0.5)$ km/s and $+(0.45, 0.25, 0.15)$ Mbar for clarity.

thickness of the Al foil was different in each experiment (see Table I) the breakout times in Fig. 3(a) are also all slightly different. Velocity steps, the result of reflected waves, can be seen clearly in cases A and B in Fig. 3(a), but become less noticeable in case C as the load is applied much more gently, a consequence of the higher density reservoir used on this shot. Case D exhibits no steps because the Al is backed by thick LiF, so the target acts much like a thick slab of Al. The backintegrated loads shown in Fig. 3(b) are smooth, but some wiggles, also due to the wave reverberations within the target, can be seen especially in case A after the peak load.

In Table I we record the peak load as well as conditions at the center of each foil from each of the LASNEX simulations. Compressions vary between $\sim10\%$ and $\sim35\%$, and the peak strain rate, which we have defined as $(\frac{1}{3} \partial \ln\rho / \partial t)$, spans an order of magnitude from $6 \times 10^7 \text{ s}^{-1}$ at the highest loading of 0.5 Mbar, to $5 \times 10^6 \text{ s}^{-1}$ at the lowest load of 0.14 Mbar. In all cases, the temperature is estimated to be approximately a factor of 5 less than the respective melt temperatures, and in the absence of other processes the conditions are essentially isentropic. We estimate the uncertainty in temperature to be $\sim5\%$ for the low pressure shot (e.g., case D) rising almost linearly to $\sim10\%$–15% for the high pressure shot (case A), by comparing results from two widely used EOS models, QEOS [24] and SESAME [25].

We have also used LASNEX to simulate the entire experiment [17]. Here we briefly compare 1D simulations that match the peak experimental load with the data (Fig. 3). We show only cases A and C for clarity. The integrated simulations compare reasonably well with the data but $P_L(t)$ rises faster, especially at the lower loading pressure. Care was taken to ensure that the computed solution for the ram pressure $[\rho u^2(t)]$ of the reservoir plasma at the sample in test calculations using perfect gas EOS matched analytic results. A softer reservoir EOS in the loading phase would lead to a slower pressure rise in the sample and is suggested by the data. The predicted loads are also slightly broader than the data resulting in slightly higher predicted velocities. In case A the higher simulated load at late time turns out to be largely a 2D effect, but in case C is most likely due to uncertainty in the EOS of the solid reservoir used. As the reservoir stagnates against the sample it becomes hot, and LASNEX predicts that a melt wave propagates slowly into the sample to a depth of ~2–4 μm by peak load, and has reached a depth of <10 μm by 100 ns later. The effect on conditions in the center of the sample (depth $> \sim8$ μm) during the VISAR window is negligible, increasing the temperature by $+2$ K (case D) up to $+10$ K (case A). For the foam reservoirs, LASNEX predicts that x-ray preheating increases the temperature in the center of the sample by up to ~150 K, but this does not occur when solid density reservoirs are used because of their relatively large optical depth. This suggests that conditions in the center of the samples driven by the solid

density reservoirs remain close to the room temperature isentrope during the experiment.

Finally we consider future prospects. For targets optimized for pressure generation with the longest rise times, analytical scaling arguments suggest that $P_L \sim P_s \sim (\omega/3)^{0.28} E^{0.43}/t^{1.37}$, where P_s is the shock pressure in the reservoir, ω is the laser light frequency relative to the fundamental ($\omega = 3$ in these experiments), and E and t are the laser energy and pulse length, respectively [17]. These optimized designs require that the laser drive remains on until the head of the rarefaction wave (traveling at the local sound speed) launched from the rear of the reservoir at shock breakout reaches the ablation front. Detailed LASNEX simulations (normalized to the experiments reported here) for optimized targets give $P_{L,\mathrm{Mbar}} = (330/\Delta^{0.9})(\omega/3)^{0.28} E_{MJ}^{0.47}/(t_{\mathrm{las}}/10 \text{ ns})^{1.5}$ which nicely reproduces the simple analytic result. In this expression Δ is the ratio of the focal spot diameter to total target length and should be >1 to preserve planarity. On a given laser facility with fixed energy, higher loads require higher laser intensities, which means shorter pulse lengths, smaller targets, and faster rise times. Eventually, the rise time becomes so fast that the compression wave steepens into a shock at a sample depth that is too small to be useful, thus placing a limit on the usable load. On the Omega laser with ~ 1 kJ of energy, such optimized targets would use ~ 30 ns laser pulses and generate ~ 2 Mbar loads. However, such long pulses are not possible on Omega and we operate in an unoptimized mode which shortens the rise time, but useful experiments should still be feasible up to ~ 1–2 Mbar in ~ 20–40 μm thick samples. The NIF laser, with its much larger energy and ability to form very long >100 ns pulses, can operate in an optimized mode and readily extends the load achievable to ~ 5 Mbar in samples that are several $\times 100$ μm thick, adequate to study bulk properties, such as EOSs and phase transitions, in a new, high-density, low-temperature regime. Experiments become increasingly challenging as the load is increased further, and the sample thickness for shockless compression drops to ~ 50 μm for an applied load ~ 10 Mbar. Additional load shaping via, for example, graded density reservoirs has yet to be explored, but could substantially increase the thickness of sample experiencing shockless loading (i.e., distance to shock formation), and may also allow even higher pressures to be reached.

[1] J. R. Asay, Int. J. Impact Eng. **20**, 27 (1997).

[2] Y. B. Zeldovich and Y. P. Raizer, *Physics of Shock Waves and High Temperature Hydrodynamic Phenomena* (Academic Press Inc., New York, 1966).

[3] F. Streitz (to be published).

[4] J. F. Barnes *et al.*, J. Appl. Phys. **45**, 727 (1974); A. I. Lebedev, P. N. Nizovtsev, and V. A. Rayevsky, in *Proceedings of the 4th International Workshop on the Physics of Compressible Turbulent Mixing* (Cambridge University Press, Cambridge, 1993); A. I. Lebedev, P. N. Nizovtsev, V. A. Rayevsky, and V. P. Solov'ev, Sov. Phys. Dokl. **41**, 328 (1996).

[5] C. A. Hall, Phys. Plasmas **7**, 2069 (2000); C. A. Hall *et al.*, Rev. Sci. Instrum. **72**, 3587 (2001); D. B. Reisman *et al.*, J. Appl. Phys. **89**, 1625 (2001).

[6] J. A. Paisner, E. M. Campbell, and W. J. Hogan, Fusion Technol. **26**, 755 (1994).

[7] H. M. Van Horn, Science **252**, 384 (1991).

[8] D. J. Stevenson, Annu. Rev. Earth Planetary Sci. **10**, 257 (1982); M. Ross *et al.*, Philos. Trans. R. Soc. London A **303**, 303 (1981).

[9] A. Laio *et al.*, Science **287**, 1027 (2000).

[10] T. Guillot, Science **286**, 72 (1999); D. Sauman, G. Chabrier, D. J. Wagner, and X. Xie, High Press. Res. **16**, 331 (2000); W. J. Nellis, Planet. Space Sci. **48**, 671 (2000); H. Mizuno, Prog. Theor. Phys. **64**, 544 (1980).

[11] W. B. Hubbard *et al.*, Phys. Plasmas **4**, 2011 (1997).

[12] E. Wigner and H. B. Huntington, J. Chem. Phys. **3**, 764 (1935); N.W. Ashcroft, Phys. Rev. B **41**, 10 963 (1990); C. Narayana *et al.*, Nature (London) **393**, 47 (1998).

[13] J. D. O'Keefe and T. J. Ahrens, J. Geophys. Res. 17 011 (1993).

[14] G. Regazzoni, U. F. Kocks, and P. S. Follansbee, Acta Metall. **35**, 2865 (1987).

[15] K. Tanaka *et al.*, Phys. Plasmas **7**, 676 (2000); M. D. Knudson *et al.*, Phys. Rev. Lett. **87**, 225501 (2001); **90**, 035505 (2003).

[16] A. G. G. M. Tielens, Astrophys. J. **499**, 267 (1998).

[17] J. Edwards (to be published).

[18] G. A. M. Renolds *et al.*, J. Non-Cryst. Solids **188**, 27 (1995).

[19] T. H. Boehly *et al.*, Rev. Sci. Instrum. **66**, 930 (1995).

[20] S. G. Glendinning *et al.*, Phys. Plasmas **10**, 1931 (2003).

[21] L. M. Barker and R. E. Hollenback, J. Appl. Phys. **43**, 4669 (1972); P. M. Celliers *et al.*, Appl. Phys. Lett. **73**, 1320 (1998).

[22] D. Hayes, Sandia Report No. SND2001-1440, 2001.

[23] G. B. Zimmerman and W. L. Kruer, Comments Plasma Phys. Control. Fusion **2**, 51 (1975).

[24] R. M. More, K. H. Warren, D. A. Young, and G. B. Zimmerman, Phys. Fluids **31**, 3059 (1988).

[25] K. S. Holian, T-4 Handbook of Material Properties Database, Vol. 1c EOS LA-10160-MS-V.1c, 1984.